

INTEGRAL SPI all-sky view in soft γ -rays: Study of point source and Galactic diffuse emissions¹

L. Bouchet, E.Jourdain, J.P.Roques

CESR-CNRS, 9 Av. du Colonel Roche, 31028 Toulouse Cedex 04, France

A. Strong, R. Diehl

*Max-Planck-Institut für extraterrestrische Physik, Postfach 1603, 85740 Garching,
Germany*

and

F. Lebrun, R. Terrier

DSM/DAPNIA/SAp, CEA-Saclay, 91191 Gif-sur-Yvette, France

APC, UMR 7164, 10 rue A. Domon et L. Duquet, 75205 Paris Cedex 13, France

Received ; accepted

ABSTRACT

We have processed the data accumulated with *INTEGRAL* SPI during 4 years (~ 51 Ms) to study the Galactic “diffuse” emission morphology in the 20 keV to 8 MeV energy range. To achieve this objective, we have derived simultaneously an all-sky census of emitting sources and images of the Galactic Ridge (GR) emission. In the central radian, the resolved point source emission amounts to 88%, 91% and 68% of the total emission in the 25-50, 50-100 and 100-300 keV domains respectively. We have compared the GR emission spatial distribution to those obtained from CO and NIR maps, and quantified our results through latitude and longitude profiles. Below 50 keV, the SPI data are better traced by the latter, supporting a stellar origin for this emission. Furthermore, we found that the GR emission spectrum follows a power law with a photon index ~ 1.55 above 50 keV while an additional component is required below this energy. This component shows a cutoff around 30 keV, reinforcing a stellar origin, as proposed by Krivonos et al. (2007).

The annihilation diffuse emission component is extracted simultaneously, leading to the determination of the related parameters (positronium flux and fraction). A specific discussion is devoted to the annihilation line distribution since a significant emission is detected over a region as large as $\sim 80^\circ$ by $\sim 10^\circ$ potentially associated with the disk or halo surrounding the central regions of our Galaxy.

Subject headings: Galaxy: general — Galaxy: structure — gamma rays: observations — surveys — (ISM): cosmic rays — ISM:general

1. Introduction

The soft γ -ray GR Emission (> 20 keV) has been previously studied essentially with the CGRO and GRANAT missions (Purcell et al., 1996, Skibo et al., 1997, Kinzer, Purcell & Kurfess, 1999). The main conclusion was that point sources explain at least 50 % of the total emission up to ~ 200 keV, allowing the possibility to anticipate that unresolved sources could explain a major part of what was seen as “diffuse continuum emission”. Soon after its launch, first INTEGRAL results indicated that the GR diffuse emission is less than 15 % of the total in the 20-200 keV domain (Lebrun et al., 2004, Terrier et al., 2004, Strong et al., 2005, Bouchet et al., 2005). In more recent works, Revnivtsev et al. (2006), with RXTE PCA data, and Krivonos et al. (2007), using the data collected with the *INTEGRAL* IBIS telescope, suggest that the GRXE (Galactic Ridge X-ray Emission) between 3 and ~ 60 keV is explained in terms of sources belonging to the population of accreting white dwarfs binaries.

In a previous paper using one year of SPI data (Bouchet et al., 2005, hereafter paper I), we had used Galactic tracer morphologies to extract the spectrum of the diffuse continuum emission as well as that of the positronium/annihilation in the central radian of our Galaxy. We thus derived the relative contributions of these emissions along with that of the point source emission to the total Galactic emission. In this paper, we present a global view of the soft γ -ray sky emission based on a larger amount of data covering the whole sky and perform an imaging analysis of the diffuse component, with an estimate of its spectrum between 20 keV and 8 MeV.

2. Instrument and Observations

The ESA’s INTEGRAL (INTERnational Gamma-Ray Astrophysics Laboratory) observatory was launched from Baikonour, Kazakhstan, on 2002 October 17. The spectrometer SPI (Vedrenne et al., 2003) observes the sky in the 20 keV - 8 MeV energy range with an

¹Based on observations with INTEGRAL, an ESA project with instruments and science data centre funded by ESA member states (especially the PI countries: Denmark, France, Germany, Italy, Spain, and Switzerland), Czech Republic and Poland with participation of Russia and USA.

energy resolution ranging from 2 to 8 keV. It consists in an array of 19 high purity Germanium (Ge) detectors operating at 85 K. Its geometrical surface is 508 cm^2 with a thickness of 7 cm. In addition to its spectroscopic capability, SPI can image the sky with a spatial resolution of 2.6° (FWHM) over a field of view of 30° , thanks to a coded mask located 1.7 m above the detection plane. Despite such a modest angular resolution, it is possible to locate intense sources with an accuracy of few arc minutes (Dubath et al., 2005). The assembly is surrounded by a 5-cm thick BGO shield which stops and measures the flux of particles arriving from outside the FoV. The instrument in-flight performance is given in Roques et al. (2003).

Due to the small number of detectors, SPI imaging capability relies on a specific observational strategy, based on a dithering procedure (Jensen et al., 2003): the pointing direction varies around the target by steps of 2° within a 5×5 square or a 7-point hexagonal pattern. In general, a pointing lasts 40 minutes, and along its 3-day orbit, INTEGRAL can be operated $\sim 85\%$ of the time outside the radiation belts.

We have analysed observations recorded from 2002, February to 2006 May, covering the entire sky (Fig. 1). The central region of the Galaxy, within $-50^\circ \leq l \leq 50^\circ$, $-25^\circ \leq b \leq 25^\circ$, is thus particularly well scanned.

Data polluted by solar flares and radiation belt entries are excluded. After image analysis and cleaning, we obtained 51×10^6 seconds of effective observing time.

3. Technical considerations and algorithm descriptions

The analysis method used in this paper is similar to the one described in our 'paper I', with some significant enhancements however. We first summarize the analysis method basics, consisting of an iterative procedure between source position determination (with SPIROS) and flux extraction (with Time-Model-Fit) steps.

- Source catalogues are iteratively produced using the SPIROS software (Skinner & Connell, 2003), in several energy bands.

An iterative search is performed for point sources, starting from the strongest one identified, and successively adding weaker ones in successive iterations. Each time a source is found in a search of trial positions on the sky, it is added to a working source catalogue, and then used as baseline knowledge for the next source search in the following iteration.

In order to avoid unnecessary artifacts from spatial-resolution limits of our instrument, for each newly-found source an identification step is introduced, and, for sufficient proximity, the (more accurate) position of the identified source is used instead.

In crowded regions, due to the 2.6° SPI angular resolution, the brightest sources are considered as representative of the local emissions. For the central degree of the Galaxy good fits have been obtained in paper I, considering 1E 1740-2942.7 only. The better statistic of our new set of data requires a more complex description of this region. Thus two other (softer) sources have been considered below 200 keV, tentatively identified with SLX 1744-299 and IGR J17475-2822.

- Using the SPIROS output catalogues, source fluxes and diffuse emission intensity distribution are derived with Time-Model-Fit (see Paper I) algorithm.

Time-model-fit algorithm is a model fitting procedure based on the likelihood/ χ^2 statistics. We thus model the sky successively with a set of three models for the large-scale diffuse and extended emission plus the sources accumulated in the search, allowing for intensity variations down to the time scale of individual pointings (~ 2000 sec) for the brightest point sources as well as for background. This latter high variability time scale is not needed normally, in particular our background rates are usually quite stable; but for cases such as solar flare events this flexibility has proven useful. For each energy band, the Time-model-fit algorithm determines the (time dependent) flux normalisation for point sources, extended emissions and background. Diffuse components and strong variable sources contributions are then subtracted from the data to produce a "corrected" data set used as SPIROS input for the next iteration.

With such flexibility, and simultaneous analysis of more than four years of data, the number of free parameters in such fitting approach can easily grow out of hand. Major improvements have been carried out, therefore:

- The matrix associated with the imaging transfer function is sparse with only a few percents of non-zero elements. We take advantage of this property by minimizing the storage and speeding-up the numerous matrix-vector operations through a Compressed Column Storage scheme (Duff et al. 1989). In addition, the transfer function related to a variable source exhibits a peculiar structure which allows a direct inversion of a part of the matrix. Thanks to these optimisations the algorithm is able to handle many more observations together with more free parameters e.g. for source variability.
- The background determination has been refined: We decompose background variability to global intensity variation and into the pattern of rates among the 19 detectors of our camera. We retain freedom of variability for global background intensity as described above, and allow the general background count rate pattern in the SPI camera to vary on a much more restrictive time scale (on the order of months). We find that over 6 months of data, no pattern variations are noticeable. With this compromise of allowing

high variability for intensity parameters of model components, and modest variability allowance for the background pattern, we obtain adequate fits to our measurements with a minimum number of parameters.

- The total energy redistribution matrix is included for the final flux extraction, with the proper spectral shape taken into account for each source and diffuse component.
- The algorithm is able to handle a sky described by cells of various sizes whose intensities are determined together with the other parameters. The use of "large" cells is suitable to gather flux from diffuse emissions in a model independent way.

This hybrid reconstruction algorithm takes the best of methods to map point source and extended emissions simultaneously . It is the basis for the results presented in this paper.

4. Mapping the sky

The GR emission is difficult to measure since its surface brightness and its signal-to-noise ratio are low. Moreover, as the distribution of a population of weak unresolved point sources formally mimics an extended structure, the goal of any diffuse emission study consists in estimating always better the source component in order to derive upper limits for the GR emission.

In paper I, the small amount of data, covering only the central radian of the Galaxy, justified the global model-fitting approach to estimate the different contributions : The GR Emission was tentatively described with a CO map while the annihilation process (511 keV line and positronium continuum) was modeled by an azimuthally symmetric Gaussian of 8° FWHM (following previous works by Knöldlseder et al., 2005).

In this paper, we attempt to estimate a model-independent GR emission morphology, by extracting local fluxes without spatial model. For this, the sky will be represented by "large" cells of fixed sizes (tested values range from 2° to 16°) whose intensities are fitted to the data through the likelihood maximisation method, together with the ponctual sources ones.

This represents the best trade off between a priori (model dependent) information introduced in the model-fitting algorithm (positions of a catalog of known sources plus variability timescale of each source) and model independent results (fluxes of sources and of cells of the extended emission).

The first step consists thus to build a catalog of individual sources as complete as possible, following the procedure used in Paper I. Then, large cells are added in the convergence process to obtain the diffuse emission distribution.

4.1. Source catalogue

We used the method described in paper I to generate source catalogues: the SPIROS software delivered in the INTEGRAL OSA (Off-line Scientific Analysis) package is used iteratively in conjunction with our hybrid algorithm. The latter calculates variable source flux contributions using Galactic tracers models for spatial morphologies of the interstellar emissions (8° axisymmetric Gaussian for the annihilation emission, DIRBE 4.9 μ and CO maps for the GR continuum below and above 120 keV respectively), for which a normalisation factor is adjusted during the fitting process. The extended emission and variable point source contributions are then removed from the data set provided to SPIROS for the next iteration. It should be noted that the point source fluxes remain the same (within error bars) whatever the GR continuum distribution model is used (CO or DIRBE), as expected given the low surface brightness of this component.

As explained in paper I, to minimize the error bars (maximize the signal-to-noise ratios), we need to describe the sky with a minimum number of free parameters. We thus define a sky model for each of the energy bands. In practice, 12 sources (marked with '*' in table I) have been considered as variable for the 25-50 keV band. Above 50 keV, the reduced χ^2 being sufficiently close to 1, only Cyg X-1 is set variable up to 200 keV.

Figure 2 displays the resulting sky images sum of point sources and “diffuse” components in different energy bands and illustrates their evolution. At low energy, the sky emission is dominated by sources while a ”diffuse/extended” structure appears above 200-300 keV, in a domain corresponding to the annihilation radiation. We will come back to it in the next section, dedicated to the diffuse emissions. Above 511 keV, sources again dominate the sky emission.

The resulting catalogues contain 173, 79, 30 and 12 sources detected above $\sim 3.5\sigma$ in the 25-50 keV and the 50-100 keV bands and above $\sim 2.5\sigma$ in the 100-200 keV and 200-600 keV ones (see Table I). All of them except one are associated (within 1°) with at least one IBIS source (Bird et al., 2006).

Above 600 keV only the Crab Nebula, Cyg X-1, GRS1915+115 and GRS1758-258 are detected, the 2 former being still emitting above 2 MeV.

Note that the reported fluxes are four years averaged values, and that this analysis is not optimised for any particular source, since all data are adjusted simultaneously. An individual source analysis should be based on a restricted number of exposures, selected on the basis of the pointing direction (typically less than $\sim 12^\circ$ relatively to the source direction), and requires a detailed study of the source time evolution.

4.2. GR Diffuse emission

4.2.1. morphology

Once the contribution of the individual sources has been independently estimated, we can study the unresolved component. The a priori information will thus now be introduced in the source terms. To determine the spatial distribution of the Galactic Ridge emission, we have considered the region $|l| < 100^\circ$, $|b| < 20^\circ$ and divided it into cells of size $\delta l = 16^\circ \times \delta b = 2.6^\circ$, the 511 keV line case being treated apart. These cell or pixel sizes have been chosen a posteriori to optimize the signal-to-noise ratio per cell while being sufficiently small to follow the observed spatial variations. We use the a priori information on the source positions obtained in the previous step, whereas the “diffuse” pixel cells, sources and background intensities are to be fitted to the data. The number of unknowns is high but reasonable compared to the data and the problem is easily tractable by a simple likelihood optimisation to determine all the corresponding intensities and error bars.

Figure 3 displays the images obtained through this method for the “diffuse” component(s) in different energy bands. The last one contains the ^{26}Al 1.8 MeV line but it is clear that its contribution to the large band flux is quite negligible.

To quantify more easily the behavior of the diffuse emission, we present our results in terms of longitude and latitude profiles (figures 4 and 5). They have been built by integrating the flux measured for $|b| < 6.5^\circ$ or $|l| < 24^\circ$, in longitude and latitude bins respectively. We can then compare them to those obtained from CO (Dame et al. 2001) and NIR Dirbe 4.9 μ corrected from reddening (<http://lambda.gsfc.nasa.gov>) maps.

Both models agree grossly with SPI longitude profiles, showing a slowly decreasing intensity of the GR emission toward high longitudes.

The latitude profiles are not so similar: Up to ~ 100 keV, the GR high energy and NIR emissions seem to be concentrated in a region slightly more extended than the CO one. This is supported by calculating a χ^2 between the resulting sky images and the proposed models. We obtained χ^2 values of 74 and 86 (37 dof) in the 25-50 keV energy band, while in the 50-100 keV energy band, chisquare values are of 50 and 53 for DIRBE and CO maps, respectively. This fits in with the current understanding of a stellar origin for the GR emission in the X ray domain (< 50 keV) proposed by Krivonos et al. (2007). However, at energies below 50 keV, systematic effects from instrumental properties and/or variability of the sources provides limitations to fit quality.

The signal to noise ratio has a minimum in the 600 keV-1.5 MeV domain, prohibiting

any serious analysis but at high energies (> 1.8 MeV), the SPI data analysis shows clearly that the diffuse emission is detected up to several MeV. All the compared spatial distributions are here compatible but the expectation is that the high energy GR diffuse emission coincides with the CO regions, where CR interact.

A deeper analysis has been performed for the annihilation line emission morphology. A 505-516 keV sky map has been built using cells of size $\delta l = 5^\circ \times \delta b = 5^\circ$ (fig. 6). In this narrow energy range, the emission is almost entirely due to the annihilation line, the contribution of the other components being negligible. The emission profiles (figures 7 and 8) are peaked towards the Galactic Centre. This structure, corresponding to the bulge, has been modeled with an axisymmetric Gaussian of $8.0^\circ \pm 0.9^\circ$ in good agreement with previous *INTEGRAL* SPI results (e. g. Knölseder et al. (2005)). However, the map together with the profiles suggest that the emission is not limited to that structure but exhibits an additional extended component revealed by the long exposure.

To quantify this result, we attempted to describe the extended spatial distribution superimposed to the central bulge, with various models. Simple geometrical shapes (ie two-dimensional Gaussians) have been tested as well as maps obtained in other wavelengths (CO and DIRBE maps). The best results are obtained with NIR data (more precisely the 3.5 to 240μ maps, too close to be differentiated in these tests) which, independently, happen to be good tracers of the ^{26}Al line emission (Knölseder et al., 1999).

For a sky model consisting of the 240μ map plus a 8° axisymmetric Gaussian, we obtain fluxes of $1.7 \pm 0.3 \times 10^{-3}$ photons $cm^{-2} s^{-1}$, in the extended structure and $0.87 \pm 0.06 \times 10^{-3}$ photons $cm^{-2} s^{-1}$ in the central one. Even though it is difficult to describe the emission in more detail, this represents a good indication for a bulge/disk structure.

Coming back to the central bulge emission, we also tested several possibilities as we suspect a geometry more complex than a single axisymmetric gaussian. A precise study of its morphology would require a specific analysis, but first investigations show that the fluxes corresponding to each structure vary within the error bars.

4.2.2. Central radian Spectrum

The spectral shape of the diffuse continuum remains of prime importance to determine its origin. As this emission is concentrated in the central regions, the spectral analysis has been restricted to the Galactic central radian ($|l| < 30^\circ$ and $|b| < 15^\circ$).

The “diffuse” continuum spectrum shown in fig 9 has been extracted assuming a NIR 4.9μ spatial distribution (up to 120 keV) and a CO map (above 120 keV) and fitted with 3

components.

- The diffuse spectrum (apart from positronium) is fitted by a power law of index 1.55 ± 0.25 , with a 100 keV flux of $4.8 \pm 0.6 \times 10^{-5} \text{ photons cm}^{-2} \text{ s}^{-1} \text{ keV}^{-1}$.
- The additional component below ~ 50 keV presents a curved shape, which can be modeled by a power law of index fixed to 0 with an exponential cutoff at 7.5 ± 1 keV and a 50 keV flux of $6.6 \pm 0.5 \times 10^{-5} \text{ photons cm}^{-2} \text{ s}^{-1} \text{ keV}^{-1}$. These parameters differ from those derived in Paper I, since many more sources have been identified, and thus removed from 'diffuse' component. This remaining "diffuse" low energy component, with a central radian luminosity of $\sim 1 \times 10^{37} \text{ erg.s}^{-1}$, is likely to correspond to the population of accreting magnetic white dwarfs proposed to provide a dominant contribution to the Galactic X-ray emission (Krivonos et al., 2007).
- The third component is due to the positronium/annihilation emission with its characteristic shape. We extract it using a 8° Gaussian spatial distribution and obtained a 511 keV line flux of $8.68 \pm 0.61 \times 10^{-4} \text{ photons cm}^{-2} \text{ s}^{-1}$. A fit to the data allows us to determine a positronium flux of $3.6 \pm 0.42 \times 10^{-3} \text{ photons cm}^{-2} \text{ s}^{-1}$ corresponding to a positronium fraction (as defined by Brown and Leventhal, 1987) of $F_p = 0.98 \pm 0.05$.
- The 511 keV emission component reveals a disk component in addition to the well-known bright bulge. We estimate a bulge-to-disk ratio of ~ 0.5 .

Above results, synthetized in Table 2, are consistent with our results in Paper I (except for the newly-found disk component at 511 keV).

5. Sources vs diffuse emission contribution

In Fig 9 we compare the different contributions to the Galactic emission : The total point source emission spectrum has been built by adding spectra from all sources detected between $|l| < 30^\circ$ and $|b| < 15^\circ$. It can be roughly described between 20 keV and 1 MeV by a power law with a photon index of 2.67 and a flux at 50 keV of $2.47 \times 10^{-3} \text{ photons cm}^{-2} \text{ s}^{-1} \text{ keV}^{-1}$. The diffuse emission is represented together with its 3 components.

From the analysis presented above, we can deduce ratios of combined emission of detected sources to the total emission of 88%, 91% and 68% in the 25-50, 50-100 and 100-300 keV bands respectively. These values represent lower limits as a population of weak unresolved sources may be confused with a diffuse emitting structure.

6. Discussion

The unresolved/extended emission observed in the soft γ -ray domain comprises three separate components: The electron-positron interactions are known to produce a large scale emission. In another hand, an interstellar emission is expected due to high energy particles travelling inside the whole galaxy. The third component has been identified more recently, with a contribution exponentially decreasing above 10 keV. We discuss each of them in the following sections.

6.1. e^-/e^+ interaction

Between 300 and 511 keV, the annihilation process plays the major role. We have determined a 511 keV flux of $8.7 \pm 0.6 \times 10^{-4} \text{ photons cm}^{-2} \text{ s}^{-1}$ and a positronium fraction $F_p = 0.98 \pm 0.05$. Comparison with previous results is quite satisfying : for example, Kinzer et al. (2001) reported a positronium fraction of 0.93 ± 0.04 in OSSE data, while independent SPI data analyses led to $F_p = 0.94 \pm 0.06$ (Churazov et al. 2005), $F_p = 0.97 \pm 0.08$ (Paper I), $F_p = 0.92 \pm 0.09$ (Weidenspointner et al., 2006) and $F_p = 0.967 \pm 0.022$ (Jean et al. 2006). Fluxes values are more difficult to compare as they depend on the assumed spatial distribution but they range around $1 \times 10^{-3} \text{ photons cm}^{-2} \text{ s}^{-1}$ in the quoted references. Indeed, the 511 keV line emission spatial distribution is essentially concentrated within the central region of the Galaxy but its morphology may be more complex than the proposed axisymmetric ($\sim 8^\circ$) Gaussian distribution. The regions surrounding this central part contain a significant flux ($\sim 1.7 \pm 0.3 \times 10^{-3} \text{ photons cm}^{-2} \text{ s}^{-1}$) which is not compatible with this simple spatial distribution. As a function of longitude, this emission seems to extend symmetrically up to $\sim 40 - 50^\circ$, while in latitude, it extends $\sim 15 - 20^\circ$. This emission could for example correspond to the disk component, as already suggested by the OSSE team (Kinzer et al. 1999). Among several models, the NIR emission distributions, otherwise considered as good ^{26}Al tracers, reveal themselves to give the best description of the SPI data in this energy domain. The mentioned link with the ^{26}Al emission leads to a straightforward interpretation: the ^{26}Al decay produces 1809 keV photons simultaneously with positrons and thus 511 keV photons in such a way that

$$\text{Flux}(511\text{keV}) = 0.85 \times (2 - 1.5 \times fp) \times \text{Flux}(1809\text{keV})$$

where fp is a positronium fraction of the annihilation process.

Using the COMPTEL measurement $\text{F}(1809 \text{ keV}) = 7 - 10 \times 10^{-4} \text{ photons cm}^{-2} \text{ s}^{-1}$ (Knölseder, 1999) and assuming fp= 0.98, we expect a 511 keV flux of $3 - 5 \times 10^{-4} \text{ photons cm}^{-2} \text{ s}^{-1}$. We thus conclude that 20-30% of the 511 keV flux emitted in the disk/halo structure could be explained by the ^{26}Al decay. The remaining $\sim 75\%$ of the observed disk/halo emission

require another origin and will be refined by adding future observations.

Previous ratio estimates of the bulge-to-disk flux ratios have been obtained with OSSE/CGRO, varying from 0.2 to 3.3 depending upon whether the bulge component features a halo (which leads to a large ratio) or not (Milne et al. 2000, Kinzer et al., 2001). Benefiting from a more uniform Galactic plane coverage than the OSSE data, the SPI data allow to better constrain this parameter. Indeed, even though the bulge-to-disk flux ratio depends on the assumed bulge and disk shapes, tests with several representative configurations lead to a bulge-to-disk flux ratio estimation of ~ 0.5 .

6.2. The < 50 keV component

This low energy component deserves a short discussion: it has been found to follow the same spatial distribution as the NIR DIRBE 4.9μ emission (see fig. 5). Together with the soft spectral shape, this corroborates the interpretation of the Galactic ridge emission between 20 and 60 keV by Krivonos et al. (2007) in terms of a population of accreting magnetic white dwarfs, which present a spectral cutoff around 30-50 keV (Suleimanov et al, 2005). Our observed luminosity of $\sim 1 \times 10^{37} \text{ erg s}^{-1}$ between 20 and 60 keV in the central radian is in good agreement with the estimation of $1.23 \pm 0.05 \times 10^{37} \text{ erg s}^{-1}$ given by Krivonos et al. (2007) on the basis of the proposed model. However, it is obviously beyond the SPI capacities (and objectives) to resolve this emission since the potential objects which could explain it are too faint, even though the global emission is clearly detected as a large scale distribution.

6.3. Interstellar emission

Above 50 keV, we detected an emission following a power law, which joins the high energy points previously measured by *CGRO* OSSE (Kinzer et al. 1999) in the MeV region (fig 10). Our photon index of $\sim 1.55 \pm 0.25$ is quite compatible with the ~ 1.75 value reported by these authors, in the 200 keV to 10 MeV domain. Krivonos et al. (2007) do not detect any Galactic Ridge Emission in the 60-200 keV range. The SPI measurements give marginal detections at those energies, fully compatible with their upper limits, as illustrated on fig 10. To go further on this point, we have to improve the determination of the source emission contribution. Indeed, if the Galactic ridge emission intensity measured with our model fitting procedure depends only slightly on the assumed spatial morphology,

the number of sources included in the sky model can lead to different results. It is clear that a population of weak sources, below the current SPI sensitivity, could contribute to the detected emission.

Still, the nature of this emission can be actually related to high energy particles. At the energies of interest to SPI the main gamma-ray emission process is inverse-Compton (IC) emission from relativistic electrons; non-thermal bremsstrahlung is of minor importance. The electrons for IC have typical energies of 1 GeV and below, and the important radiation fields are CMB, starlight and IR. A theoretical prediction in the SPI energy range using the GALPROP model (Strong & Moskalenko, 1998; Strong et al, 2004; Moskalenko et al., 2007; Strong, Moskalenko and Ptuskin, 2007) can be seen in Strong et al (2005). The general conclusion up to now has been that the IC component fails by a factor of a few to explain the observed emission.

However now in this new work, with three times as much SPI data it is possible to determine the non-thermal component with much greater accuracy, both because of increased exposure and better accounting for point sources and better handling of the instrumental background.

The result is a significantly lower intensity of the power-law component than given by Strong et al (2005), where however the error bars were much larger than now. The result is that now there is better agreement with the IC prediction, mitigating the need for other processes. In fact, the hard power law continuum is now in good agreement with predictions from the GALPROP code, which takes into account both cosmic-ray primary electrons and secondary electrons/ positrons: the hard power law continuum component can be identified with inverse Compton scattering. Detailed modelling and interpretation of the data will be given in Porter et al. (2007).

7. Conclusions

The "diffuse emission" generic term gathers a set of various processus depending on the energy domain, and making the determination of its origin rather difficult. In the soft γ -ray domain, the diffuse emission represents a complex problem, as its presence is swamped with the individual sources emission and difficult to disentangle.

To investigate it, we have developed an imaging algorithm dedicated to extended structures. This code first determines and takes into account the point sources emitting in the same energy domain, allowing us to then better estimate the geometry of the regions producing diffuse emissions.

The SPI all-sky survey analysis reveals that 173 sources can be identified in the 25-50 keV

with 30 of them emitting a significant flux ($> \sim 2.5 \sigma$) above 100 keV. It is clear now that the sources dominate the Galactic emission up to ~ 300 keV (Fig. 9). Finally, upper limits on the diffuse emission are estimated to be one tenth of the total emission below 100 keV and one third in the 100-300 keV band.

The e^-/e^+ annihilation produces an emission which has already been the subject of many studies. The main point emerging from our analysis concerns the spatial distribution of this emission since a large structure, potentially associated with the Galactic disk/halo has been found to contain a significant fraction of the 511 keV line total flux. While a deeper analysis is required to refine this result, it is clear that the $\sim 8^\circ$ Gaussian distribution previously reported does not represent the complexity of the 511 keV line emission morphology. Once the source and annihilation process contributions have been taken into account, we can access to the "diffuse" Galactic emission, whose origin remains problematic. Its morphology is of prime importance as it is thought to trace the CR electron population, observed through bremsstrahlung or Compton emission. The *INTEGRAL* SPI data allow us to investigate this particular topic, and we present for the first time images of the diffuse Galactic emission up to a few MeV.

This diffuse emission is clearly detected between 50 keV and 2 MeV with a power law relatively hard (photon index around 1.55), and an additional component, much steeper, required below 50 keV.

Toward high energy, the SPI spectrum joins with the OSSE and EGRET measurements. All together, they can be compared to various models to understand the nature of this emission. The inverse Compton interaction is a good candidate and will be investigated in a forthcoming paper. Other interstellar processes have been invoked to explain the emission below 1 MeV (Dogiel et al., 2002; Masai et al., 2002; Schröder et al., 2005). In another side, unresolved point sources are the most probable origin below 50 keV (Krivonos et al., 2007) and are also a possibility at higher energies as AXPs or other pulsars (see for example Kuiper et al. 2004; Strong, 2007). Observations of such sources up to a few MeV would allow to quantify their potential contribution and bring a new piece to the Galactic diffuse emission riddle.

Acknowledgments

The *INTEGRAL* SPI project has been completed under the responsibility and leadership of CNES. We are grateful to ASI, CEA, CNES, DLR, ESA, INTA, NASA and OSTC for support.

AWS is supported by the German Bundesministerium für Bildung, Wissenschaft, Forschung und Technologie (BMBF/DLR) under contract No. FKZ 50 OG 0502.

REFERENCES

- Bazzano A., Stephen J.B., Fiocchi M. et al., 2006, ApJ, 649, L9
Bird A.J., Malizia A., Bazzano A. et al., 2006, ApJS, 170, 175
Bouchet L., Roques J. P., Mandrou P. et al., 2005, ApJ, 635, 1115 (Paper I)
Brown B. & Leventhal M., 1987, ApJ, 319, 637
Churazov E., Sunyaev R., Sazonov S. et al, 2005, MNRAS, 357, 1377
Dame T. M., Hartmann D. & Thaddeus P., 2001, ApJ, 547, 792
Dean A.J., Hill, A. B., Stephen J. B., et al, 2005, A&A, 443, 485
Dogiel V. A., Schönfelder V. and Strong, A. W., 2002, A&A, 382, 730
Dubath P., Knöldlseder J., Skinner G.K., et al., 2005, MNRAS, 357, 420
Duff I., Grimes R. and J. Lewis, Sparse matrix test problems, ACM Trans. Math. Soft., 15 (1989), pp. 1-14.
Jean P., , et al., 2006, A&A, 445, 579
Jensen P.L., Clausen K., Cassi C., et al., 2003, A&A, 411, L7
Kinzer R.L., Purcell W.R., Kurfess J.D. et al., 1999, ApJ, 515, 215
Kinzer R.L., Milnes P.A., Kurfess J.D. et al., 2001, ApJ, 559, 282
Knöldlseder J., 1999, PhD, Université P. Sabatier, Toulouse, France
Knöldlseder J., Bennett K., Bloemen H., et al., 1999, A&A, 344, 68
Knöldlseder J., Pierre J., Lonjou V., et al., 2005, A&A, 441, 513
Krivonos R., Revnivtsev M., Churazov E. et al., 2007, A&A, 463, 957
Kuiper, L., Hermsen W. and Mendez M., 2004, ApJ, 613, 1173
Lebrun F., Terrier R., Bazzano A. et al., 2004, Nature, 428, 293

- Masai K., Dogiel V. A., Inoue H. et al., 2002, ApJ, 581, 1071
- Milne, P. A., Kurfess, J. D., Kinzer et al., 2000, AIP Conf. Proc., 510, 211
- Moskalenko I. V. et al., 2007, AIP Conf Proc 921, 490
- Porter T.A., Moskalenko I. V., Strong A. W., Orlando E. and Bouchet L., 2007, ApJ, submitted
- Purcell W.R., Bouchet L., Johnson W.N. et al., 1996, A&AS, 120, 389
- Revnivtsev M., Sazonov S., Gilfanov M. et al., 2006, A&A, 452, 169
- Roques J.P., Schanne S., Von Kienlin A., et al, 2003, A&A, 411, L91
- Schröder R., Schlickeiser R. and Strong A. W., 2005. A&A, 442, L45
- Skibo J. G., Johnson W. N., Kurfess J. D. et al., 1997, ApJ, 483, L95
- Skinner G. & Connell P., 2003, A&A, 411, L123
- Strong A. W. & Moskalenko I. V., 1998, ApJ, 509, 212
- Strong A. W., Moskalenko I. V. and Reimer O., 2004, ApJ 613, 962
- Strong A. W., Diehl R., Halloin H. et al., 2005, A&A, 444, 495
- Strong A. W., 2007, Astrophysics and Space Science, 309, 35 Proceedings of Conference 'The multi-messenger approach to high-energy gamma-ray sources', Barcelona, 2006. astro-ph/0609359v3
- Strong A. W., Moskalenko I. V. and Ptuskin V. S., 2007, Ann. Rev. Nuc. Part. Sci. 57, 285
- Suleimanov V., Revnivtsev M., & Ritter H., 2005, A&A, 435, 191
- Terrier R., Lebrun F., Belanger G. et al., 2004, Proc. 5th INTEGRAL Workshop, ESA SP-552, p513; astro-ph/0405207
- Vedrenne G., Roques J.P., Schonfelder V., et al, 2003, A&A, 411, L63
- Weidenspointner G., Knöldlseder J., Pierre J. et al, 2006, A&A, 450, 1013

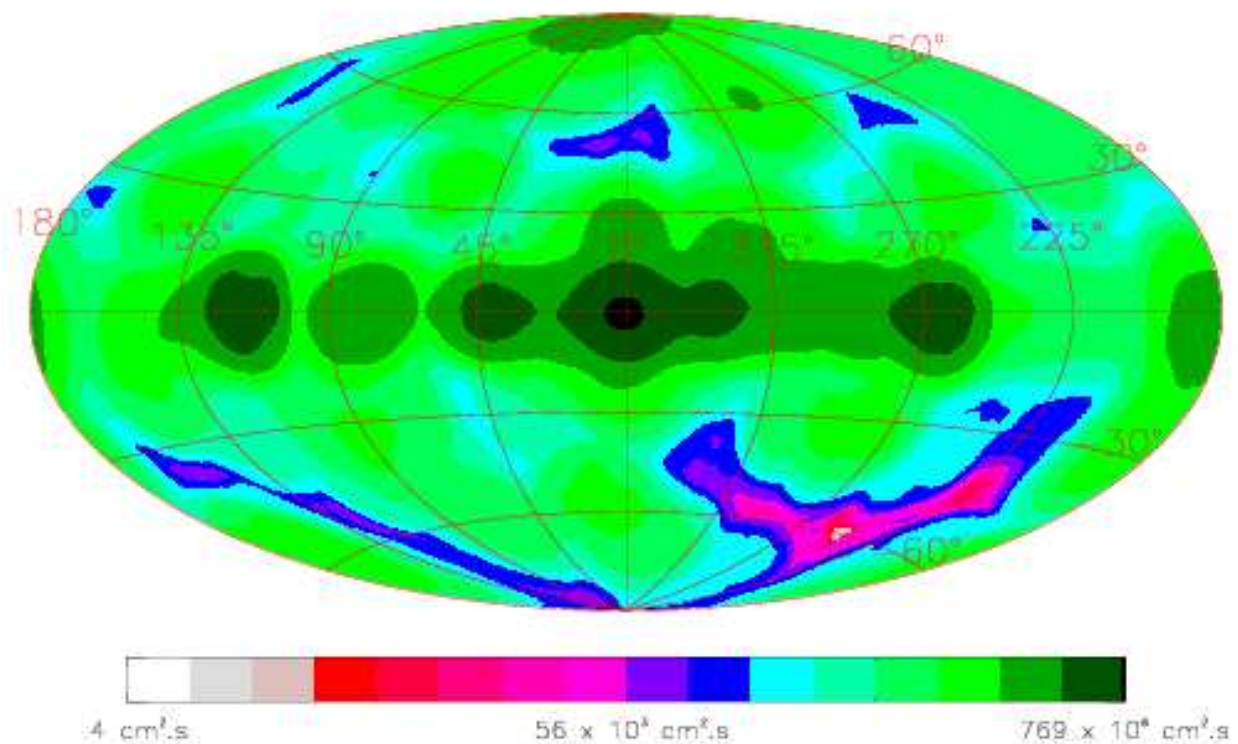


Fig. 1.— 25-50 keV *INTEGRAL* SPI exposure map. Units are in cm² s. This map takes into account the differential sensitivity of SPI accross its field of view.

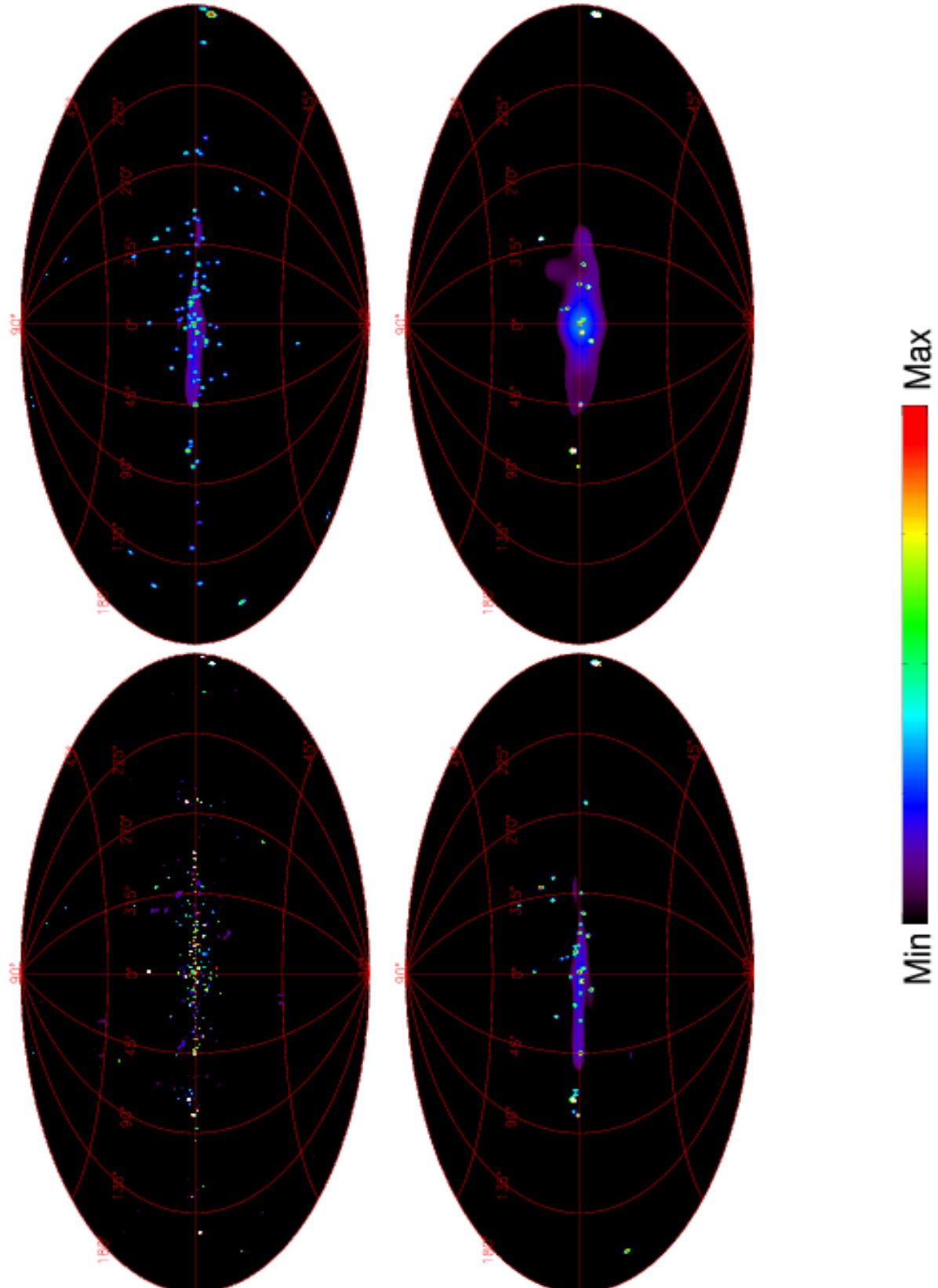


Fig. 2.— Sky-maps in the 25-50 keV (top-left), 50-100 keV (top-right), 100-200 keV (bottom-left) and 200-600 (bottom-right) energy bands. The images are scaled logarithmically with a rainbow color map (the scale of colors ranges from black (weakest intensity) to red (strongest

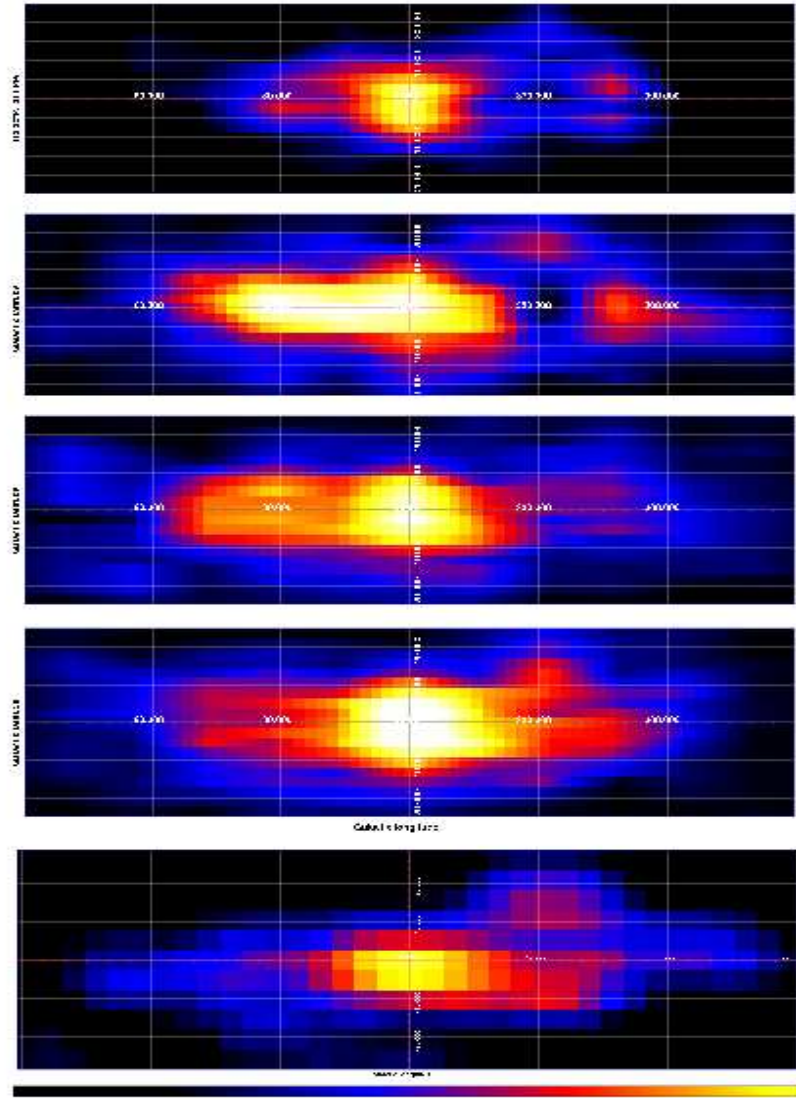


Fig. 3.— Diffuse emission morphology in different energy bands (significance maps): 25-50 keV, 50-100 keV, 100-200 keV, 200-600 keV and 1.8-7.8 MeV from up to bottom.

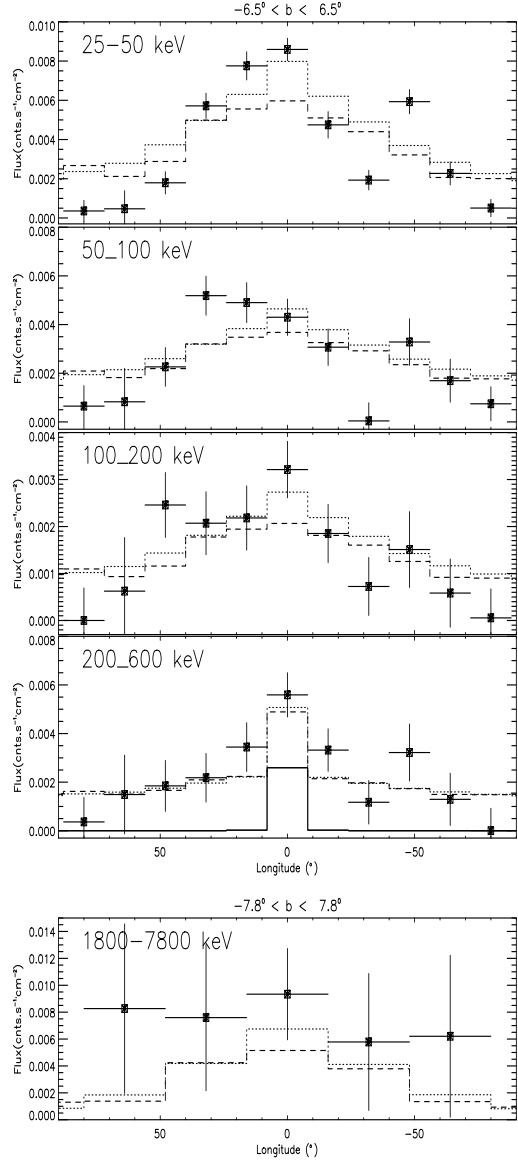


Fig. 4.— Longitude profiles in different energy bands for $|b| \leq 6.5^\circ$ (except for the last band). Dotted and dashed lines correspond respectively to the NIR 4.9 μ and CO maps. For the 200-600 keV band, the annihilation contribution (8 $^\circ$ ircgaussian distribution) is represented by the solid line.

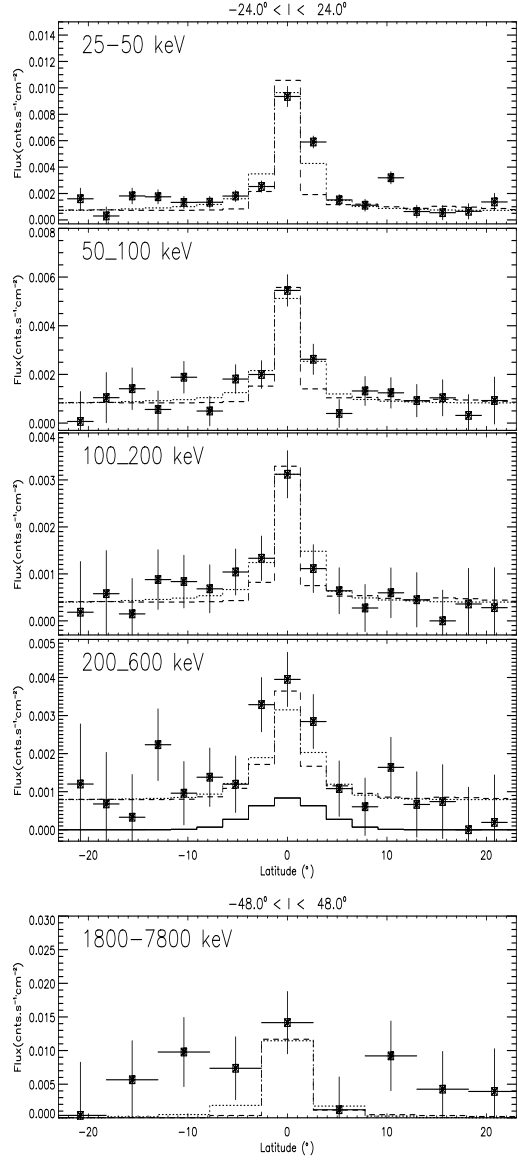


Fig. 5.— Latitude profiles in different energy bands for $|l| \leq 24^\circ$ (except for the last band). Dotted and dashed lines correspond respectively to the NIR 4.9 μ and CO maps. For the 200-600 keV band, the annihilation contribution (8° *circgaussian* distribution) is represented by the solid line.

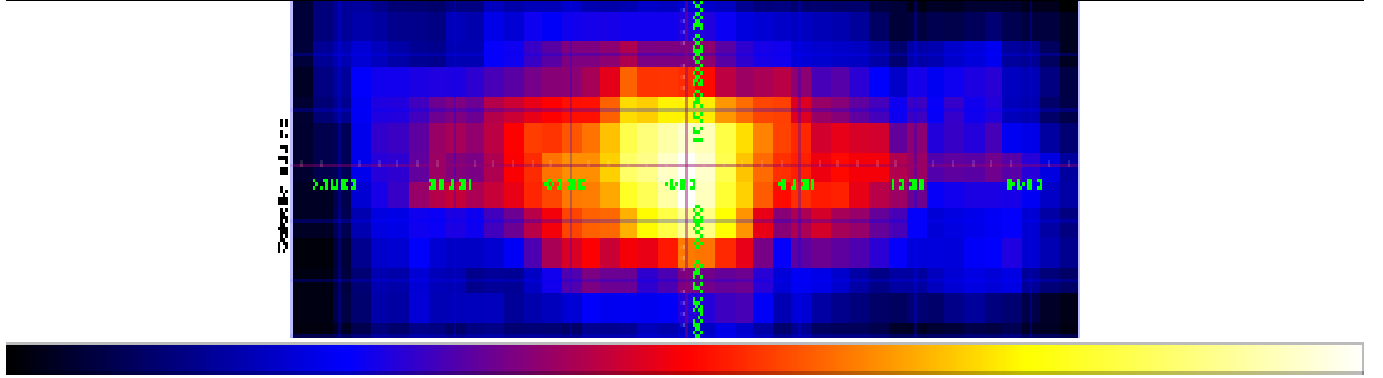


Fig. 6.— map of the significance of the 511 keV line emission

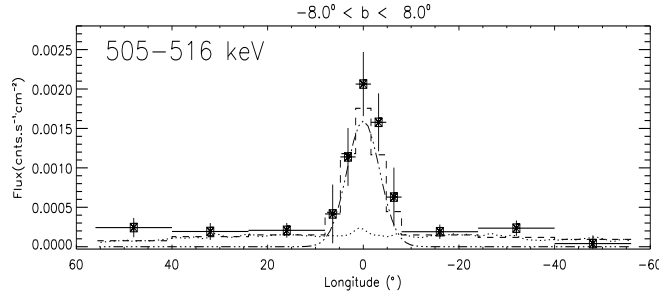


Fig. 7.— Longitude profile in the 511 keV line for $|b| \leq 8^\circ$. Dotted-dashed line corresponds to a 8° axisymmetric Gaussian. Dotted line corresponds to the extended distribution (240 μ map model). The sum of both has been integrated on the same bins as the data (histogram) to compare to them.

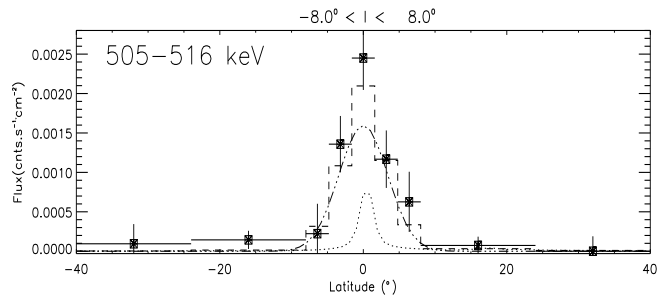


Fig. 8.— Latitude profile in the 511 keV line for $|l| \leq 8^\circ$. Dotted-dashed line corresponds to a 8° axisymmetric Gaussian. Dotted line corresponds to the extended distribution (240 μ map model). The sum of both has been integrated on the same bins as the data (histogram) to compare to them.

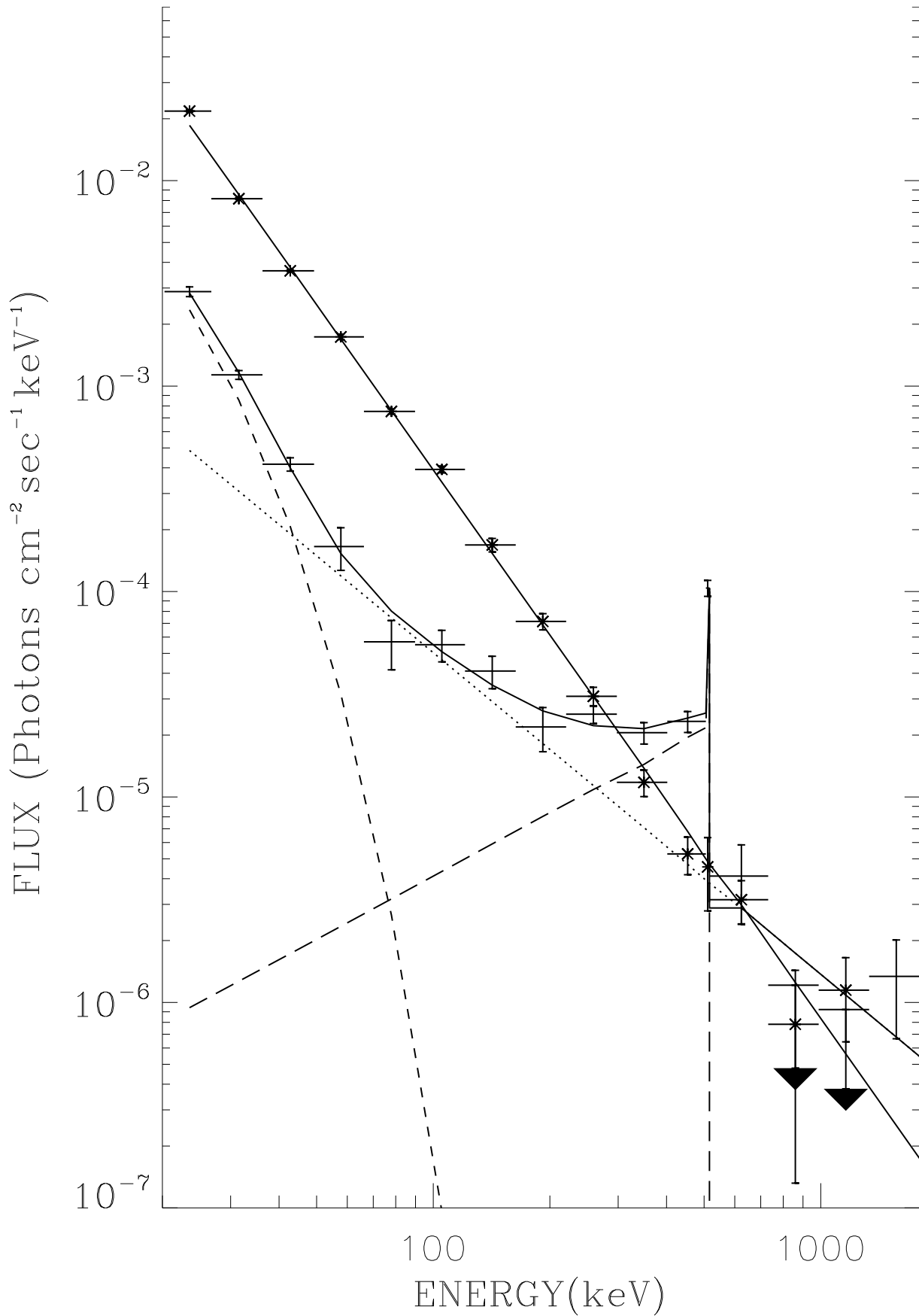


Fig. 9.— Spectra of the different emission components in the central radian of the Galaxy,

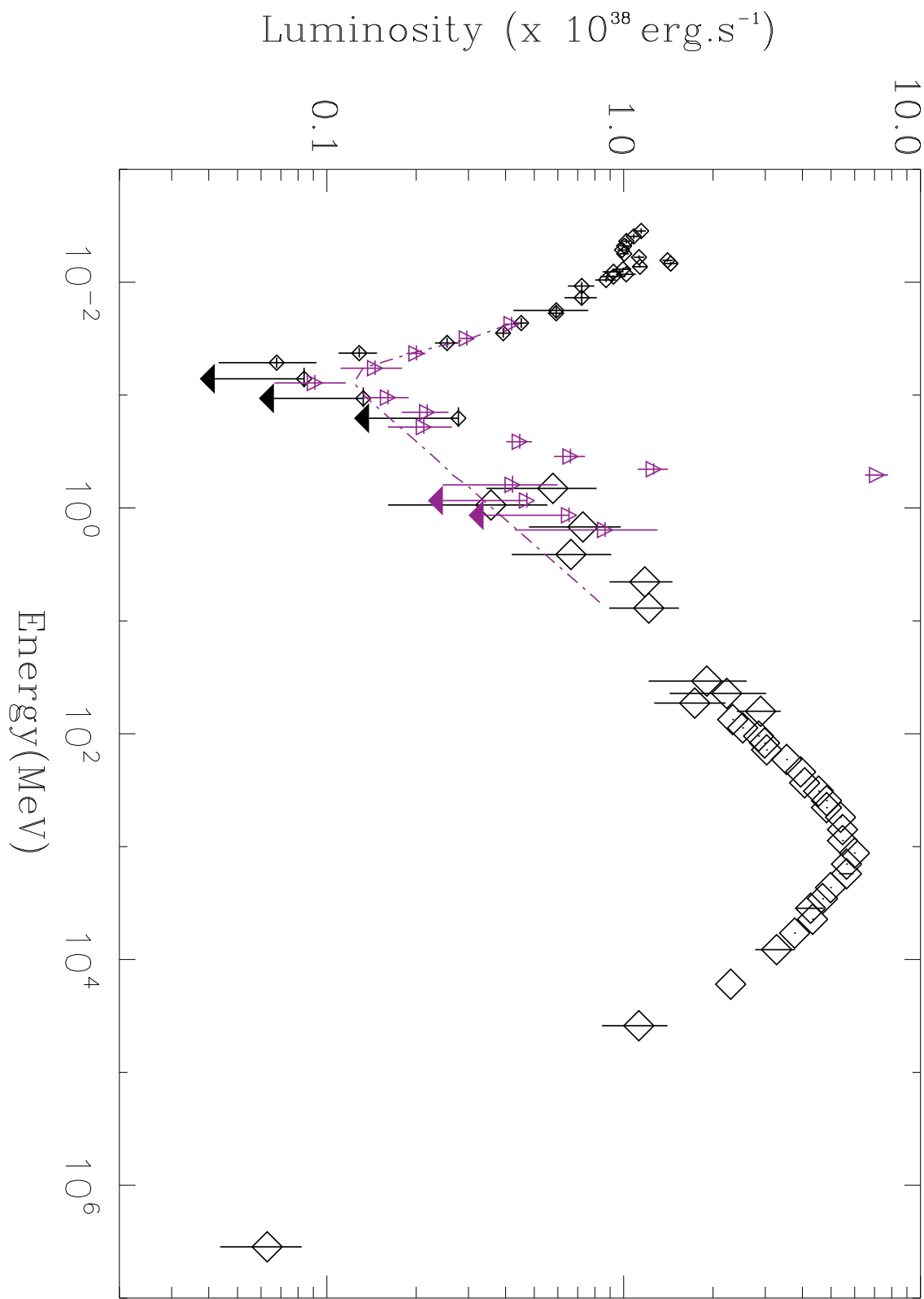


Fig. 10.— SPI all sky diffuse emission spectrum (triangles) compared to the broad band

Table 1. Sources catalogue

Name	l deg	b deg	25 - 50 keV mCrab	50 - 100 keV mCrab	100 - 200 keV mCrab	200 - 600 keV mCrab
A0535+26*	181.45	-2.6	78.4 ± 1.3	33.6 ± 2.0	< 3.9	
Crab	184.55	-5.8	1000.0 ± 0.8	1000.0 ± 1.9	1000.0 ± 3.7	1000.0 ± 8.3
4U 0614+091	200.87	-3.4	21.1 ± 1.3	13.1 ± 3.1	< 5.5	
IGR J07597-3842	254.48	-4.7	3.0 ± 0.6	5.6 ± 1.5	6.4 ± 2.7	< 12.0
IGR J07565-4139	256.68	-6.7	3.5 ± 0.5	3.5 ± 1.5	< 5.6	
4U 0836-429	261.94	-1.1	19.2 ± 0.4	13.9 ± 1.1	6.5 ± 2.2	< 10.2
IGR J09103-3741	261.97	7.0	1.8 ± 0.5	1.9 ± 1.3	< 2.5	
MCG-05-23-016	262.70	17.2	6.3 ± 1.5	5.1 ± 3.3	< 5.2	
Vela X-1*	263.05	3.9	190.4 ± 0.7	24.0 ± 1.1	3.8 ± 2.2	< 5.1
Vela pulsar	263.55	-2.8	10.8 ± 0.4	8.8 ± 1.1	12.6 ± 2.1	13.9 ± 4.9
IGR J09026-4812	268.84	-1.1	2.5 ± 0.4	< 1.1		
SWIFT J1009.3-4250	273.93	10.8	4.6 ± 0.7	2.7 ± 1.9	< 3.5	
4U0919-54	275.81	-3.9	3.0 ± 0.5	3.2 ± 1.2	< 4.6	
LMC X-4	276.33	-32.5	38.3 ± 1.3	9.6 ± 3.6	< 7.0	
NGC 4388	279.16	74.3	12.6 ± 1.2	18.4 ± 3.1	14.7 ± 5.5	< 23.6
EXO 0748-676	279.98	-19.8	16.7 ± 1.5	16.8 ± 3.7	< 6.3	
GRO J1008-57	282.98	-1.8	4.5 ± 0.5	3.5 ± 1.4	< 5.4	
IGR J09025-6814	284.17	-14.2	3.8 ± 1.0	< 2.7		
IGR J10147-6354	286.70	-6.1	2.6 ± 0.6	< 1.6		
ESO 33-2	287.84	-33.3	4.4 ± 1.2	< 3.3		
3C 273	290.00	64.3	8.5 ± 0.9	13.8 ± 2.5	9.4 ± 4.9	< 22.2
Cen X-3	292.09	0.3	30.1 ± 0.6	3.2 ± 1.5	< 5.8	
IGR J11305-6256	293.94	-1.5	2.2 ± 0.6	< 1.6		
1E 1145.1-6141	295.49	-0.0	23.2 ± 0.6	13.1 ± 1.5	< 2.8	
IGRJ12026-5349	295.72	8.4	3.2 ± 0.7	< 1.7		
NGC 4593	297.51	57.4	3.5 ± 0.9	3.6 ± 2.6	< 10.2	
XSS J12270-4859	298.97	13.8	3.3 ± 0.9	< 2.4		
NGC 4507	299.65	22.9	6.2 ± 1.3	< 3.5		
GX 301-2*	300.10	-0.0	110.2 ± 1.1	7.6 ± 1.7	< 3.4	
SMC X-1	300.39	-43.6	17.3 ± 3.0	10.4 ± 7.9	< 13.7	
4U 1246-588	302.67	3.8	6.0 ± 0.6	9.0 ± 1.6	8.4 ± 3.1	< 13.6
IGR J13020-6359	304.11	-1.1	5.2 ± 0.7	3.6 ± 1.7	< 6.4	
NGC 4945	305.27	13.3	17.6 ± 0.8	18.9 ± 2.1	14.3 ± 4.0	20.2 ± 8.3
ESO323-G077	306.02	22.3	3.7 ± 1.1	< 2.9		
4U 1323-62	307.03	0.5	10.8 ± 0.7	4.9 ± 1.8	< 3.3	
Cen A	309.51	19.4	38.2 ± 1.0	42.8 ± 2.5	56.9 ± 4.6	70.1 ± 9.8
4U 1344-60	309.76	1.5	6.0 ± 0.7	6.9 ± 1.6	4.4 ± 3.1	< 14.0
Circinus galaxy	311.32	-3.8	15.1 ± 0.7	11.8 ± 1.7	< 3.3	
IGR J14331-6112	314.90	-0.7	10.2 ± 0.6	7.0 ± 1.6	12.3 ± 2.9	< 12.8
IGR J14471-6414 ⁺	315.00	-4.1	4.2 ± 0.7	< 1.8		
IC 4329A	317.51	30.9	12.8 ± 1.1	14.9 ± 2.9	11.1 ± 5.3	< 11.5
IGR J14536-5522 ⁺	319.76	3.4	11.3 ± 0.6	12.5 ± 1.4	7.9 ± 2.8	< 6.1
PSR B1509-58	320.31	-1.2	3.8 ± 0.6	3.7 ± 1.6	9.4 ± 3.0	
4U 1626-67	321.80	-13.1	9.1 ± 1.0	4.6 ± 2.6	< 4.7	
Cir X-1	322.12	0.0	2.1 ± 0.6	< 1.5		
IGR J16377-6423	324.53	-11.5	7.2 ± 0.8	9.0 ± 1.9	< 7.0	< 7.6
IGRJ16119-6036	325.23	-6.7	4.4 ± 0.6	4.2 ± 1.5	< 2.8	
XTE J1550-564	325.88	-1.8	19.3 ± 0.5	27.6 ± 1.3	30.2 ± 2.5	18.8 ± 5.5

Table 1—Continued

Name	l deg	b deg	25 - 50 keV mCrab	50 - 100 keV mCrab	100 - 200 keV mCrab	200 - 600 keV mCrab
4U 1538-522	327.43	2.2	12.8 ± 0.5	< 1.3		
ESO 138-1	329.66	-9.5	3.6 ± 0.6	< 1.6		
4U 1608-522	330.92	-0.9	13.9 ± 0.6	7.0 ± 1.4	< 2.7	
IGR J15479-4529	332.42	7.0	7.7 ± 0.5	4.3 ± 1.2	< 4.8	
PSR J1617-5055 ⁺	332.45	-0.3	9.9 ± 0.6	8.0 ± 1.4	6.2 ± 2.3	< 10.4
4U 1636-536	332.91	-4.8	19.3 ± 0.5	9.1 ± 1.3	3.7 ± 2.5	< 5.7
IGR J16318-4848	335.61	-0.4	36.2 ± 1.2	15.4 ± 1.4	4.9 ± 2.8	< 6.3
4U 1630-47 ^a	336.91	0.2	34.4 ± 2.1	26.7 ± 1.4	21.7 ± 2.4	21.4 ± 5.3
IGR J16358-4726 ^a	337.10	0.0	6.8 ± 2.1	14.5 ± 5.5	< 10.7	
GX 339-4	338.94	-4.3	36.7 ± 0.5	40.1 ± 1.3	35.6 ± 2.4	30.0 ± 5.2
GX 340+0	339.59	-0.1	16.6 ± 0.6	3.0 ± 1.3	< 2.4	
SPI J1720-49***	340.46	-6.8	4.4 ± 0.6	11.1 ± 1.4	< 2.5	
IGR J16493-4348 ⁺	341.37	0.6	7.3 ± 0.6	2.8 ± 1.3	< 2.6	
4U 1705-440	343.32	-2.3	14.1 ± 0.7	3.6 ± 1.6	6.6 ± 3.0	< 13.8
4U 1702-429	343.87	-1.3	9.4 ± 0.7	7.7 ± 1.7	< 3.3	
OAO 1657-415	344.37	0.3	69.1 ± 0.6	33.5 ± 1.3	10.3 ± 2.2	13.0 ± 4.8
GRO J1655-40	344.98	2.5	2.0 ± 0.5	6.3 ± 1.1	9.1 ± 2.2	< 4.9
4U 1735-444	346.05	-7.0	8.4 ± 0.5	< 1.3		
IGR J17195-4100	346.98	-2.2	6.7 ± 0.5	4.8 ± 1.2	< 4.6	
4U 1700-377*	347.75	2.2	189.6 ± 0.8	103.1 ± 1.1	35.5 ± 2.2	6.4 ± 4.8
IGR J16194-2810	349.08	15.5	6.9 ± 0.8	< 1.8		
GX 349+2	349.11	2.7	8.8 ± 0.9	< 2.2		
IGR J17091-3624	349.52	2.2	7.8 ± 0.8	10.0 ± 1.0	5.6 ± 2.0	9.8 ± 4.4
IGR J16500-3307	349.71	7.3	2.5 ± 0.6	< 1.4		
Swift J1656.3-3302	350.61	6.3	3.4 ± 0.5	8.5 ± 1.0	5.0 ± 1.9	17.6 ± 4.0
IGR J17204-3554	351.27	0.7	2.5 ± 0.6	< 1.5		
IGR J16482-3036	351.43	9.2	2.7 ± 0.5	7.1 ± 1.1	5.2 ± 1.9	< 4.3
EXO 1722-363	351.50	-0.3	8.9 ± 0.6	4.3 ± 1.5	5.1 ± 2.8	
4U 1705-32	352.79	4.7	2.1 ± 0.4	3.0 ± 1.0	< 4.0	
1A 1744-361	354.12	-4.2	3.1 ± 0.6	3.4 ± 1.4	< 2.7	
GX 354-0	354.31	-0.1	34.2 ± 0.4	14.6 ± 0.9	7.6 ± 1.8	7.9 ± 4.1
XTE J1720-318 ⁺	354.62	3.1	7.6 ± 0.4	5.0 ± 0.9	< 3.4	
GRS 1724-308	356.31	2.3	17.0 ± 0.4	8.7 ± 0.9	< 3.4	
XTE J1710-281	356.35	6.9	4.8 ± 0.5	3.3 ± 1.1	< 2.2	
SLX 1746-331 ⁺	356.81	-3.0	8.0 ± 0.5	6.4 ± 1.1	< 4.4	
3A 1822-371	356.86	-11.3	19.7 ± 0.5	4.7 ± 1.1	< 4.4	
IGR J17464-3213*	357.26	-1.8	17.5 ± 0.8	13.7 ± 1.1	11.2 ± 1.6	9.9 ± 3.6
XTE J1709-267	357.48	7.9	5.0 ± 0.5	4.5 ± 1.1	2.6 ± 2.1	< 4.9
GRS 1734-294	358.90	1.4	11.7 ± 0.5	7.4 ± 1.0	6.1 ± 2.1	< 4.7
Sco X-1*	359.09	23.8	205.1 ± 1.2	16.4 ± 1.9	11.5 ± 3.8	< 8.2
1E 1740.7-2942	359.12	-0.1	49.6 ± 1.0	52.5 ± 1.2	48.3 ± 1.6	39.2 ± 3.6
SLX 1744-299	359.28	-0.9	16.9 ± 0.8	8.6 ± 2.1	< 8.2	
XTE J817-330	359.82	-8.0	7.3 ± 0.4	6.6 ± 0.9	4.7 ± 1.7	< 7.8
V2400 Oph	359.86	8.7	6.7 ± 0.7	< 1.7		
Oph Cluster	0.59	9.3	4.4 ± 0.7	2.6 ± 1.7	< 3.2	
IGR J17475-2822	0.61	-0.1	32.9 ± 0.5	20.2 ± 1.1	< 4.6	
SLX 1735-269	0.79	2.4	12.4 ± 0.4	7.7 ± 0.9	< 1.8	
RX J1832-330	1.53	-11.4	8.9 ± 0.5	6.7 ± 1.0	7.7 ± 2.0	< 9.0

Table 1—Continued

Name	l deg	b deg	25 - 50 keV mCrab	50 - 100 keV mCrab	100 - 200 keV mCrab	200 - 600 keV mCrab
GX 1+4	1.93	4.8	48.3 ± 0.4	32.8 ± 0.9	6.2 ± 1.7	< 3.5
GX 3+1	2.30	0.8	4.6 ± 0.5	2.8 ± 1.1	< 2.3	
4U 1820-303	2.78	-7.9	11.6 ± 0.4	1.4 ± 1.0	< 4.0	
GRS 1758-258	4.50	-1.4	62.3 ± 0.7	79.2 ± 1.7	83.4 ± 1.6	47.4 ± 3.6
V1223 Sgr	4.97	-14.3	5.8 ± 0.6	< 1.5		
GX 5-1	5.08	-1.0	20.4 ± 0.8	4.2 ± 1.7	< 3.4	
V2487 Oph	6.59	7.8	2.1 ± 0.5	< 1.1		
IGR J18173-2509	6.78	-4.3	3.1 ± 0.4	3.2 ± 0.9	< 3.4	
IGR J17597-2201	7.56	0.8	3.3 ± 0.8	4.1 ± 1.9	5.1 ± 3.6	
IGR J17586-2129	8.05	1.3	4.1 ± 0.9	2.5 ± 2.2	< 4.2	
IGR J17513-2011	8.17	3.4	2.8 ± 0.4	3.1 ± 1.0	< 2.0	
GX 9+9	8.50	9.0	4.0 ± 0.5	< 1.2		
GS 1826-24	9.27	-6.1	83.1 ± 0.4	66.1 ± 1.0	33.6 ± 1.9	24.5 ± 3.9
SAX J1802.7-201	9.42	1.0	8.1 ± 0.6	< 1.6		
SGR 1806-20	9.98	-0.2	5.4 ± 0.6	4.0 ± 1.2	< 2.4	
PSR J1811-1926 ^b	11.17	-0.3	3.7 ± 0.6	7.7 ± 1.2	6.3 ± 1.8	< 8.0
HETE J1900.1-2455	11.30	-12.9	15.8 ± 0.7	10.9 ± 1.5	7.1 ± 2.8	< 6.0
PKS 1830-211	12.17	-5.7	3.8 ± 0.5	5.4 ± 1.1	4.3 ± 2.1	< 9.4
IGR J18135-1751 ⁺	12.79	0.0	4.6 ± 0.9	4.4 ± 2.3	< 4.5	
GX 13+1	13.52	0.1	8.1 ± 0.9	6.6 ± 2.2	< 4.3	
2E 1739.1-1210	13.93	9.4	4.5 ± 0.6	6.6 ± 1.3	< 4.8	
NGC 7172	15.12	-53.1	6.9 ± 1.6	12.1 ± 4.4	< 8.6	
GX 17+2	16.43	1.3	20.6 ± 0.8	< 1.9		
AX J1820.5-1434	16.48	0.1	3.5 ± 0.8	4.7 ± 1.9	< 7.4	
IGR J18214-1318	17.69	0.5	3.8 ± 0.7	2.6 ± 1.9	< 3.6	
M 1812-12	18.03	2.4	25.9 ± 0.6	24.2 ± 1.3	12.9 ± 2.4	< 5.0
IGR J183047-1232	19.44	-1.2	3.2 ± 0.6	3.4 ± 1.5	< 5.8	
SNR 021.5-00.9	21.51	-0.9	4.9 ± 1.0	3.4 ± 2.5	< 4.8	
AX J183039-1002 ⁺	21.67	0.0	4.4 ± 1.0	3.7 ± 2.5	< 4.8	
IGR J18325-0756	23.71	0.6	3.5 ± 0.7	4.8 ± 1.8	4.9 ± 3.4	
SWIFT J1753.5-0127*	24.90	12.2	12.4 ± 1.3	18.4 ± 2.0	14.5 ± 3.5	< 7.6
AX J1838.0-0655	25.26	-0.2	4.4 ± 0.7	3.9 ± 1.9	< 3.7	
4U 1850-087	25.35	-4.3	8.7 ± 0.6	4.1 ± 1.5	< 5.8	
AX J1841.0-0535 ⁺	26.77	-0.2	7.9 ± 0.7	10.2 ± 1.3	11.5 ± 2.5	< 11.0
RX J1940.1-1025 ⁺	28.98	-15.5	9.8 ± 1.3	8.3 ± 2.7	< 9.4	
IGR J18483-0311 ⁺	29.75	-0.7	7.6 ± 1.0	< 5.2		
4U1822-000	29.94	5.8	2.4 ± 0.7	< 1.5		
3A 1845-024	30.42	-0.4	4.4 ± 1.1	< 5.8		
XTE J1855-026	31.08	-2.1	11.4 ± 0.6	6.8 ± 1.3	2.9 ± 2.5	< 5.7
4U 1916-053	31.35	-8.5	7.2 ± 0.7	7.6 ± 1.5	8.8 ± 2.9	< 6.4
IGR J18485-0047	31.90	0.3	6.2 ± 0.7	7.0 ± 1.2	2.5 ± 2.4	< 5.5
GS 1843+009	33.05	1.7	4.7 ± 0.6	2.2 ± 1.4	< 5.4	
XTE J1901+014	35.37	-1.6	4.3 ± 0.6	3.0 ± 1.4	< 2.6	
Aql X-1*	35.71	-4.1	16.6 ± 0.8	13.9 ± 1.2	5.8 ± 2.3	< 5.3
Ser X-1	36.12	4.8	3.1 ± 0.5	1.5 ± 1.3	< 2.5	
XTE J1858+034	36.82	-0.1	10.3 ± 0.7	4.3 ± 1.6	< 6.4	
4U 1901+03	37.18	-1.3	14.1 ± 0.7	< 1.7		
SS 433	39.69	-2.2	6.5 ± 0.5	2.7 ± 1.2	< 5.6	

Table 1—Continued

Name	l deg	b deg	25 - 50 keV mCrab	50 - 100 keV mCrab	100 - 200 keV mCrab	200 - 600 keV mCrab
4U 1909+07	41.90	-0.8	11.1 ± 0.5	4.7 ± 1.3	< 5.0	
XTE J1908+094 ⁺	43.27	0.4	14.1 ± 0.7	2.7 ± 1.6	< 6.4	
IGR J19140+0951	44.29	-0.5	8.6 ± 0.9	11.4 ± 1.7	< 3.3	
GRS 1915+105*	45.36	-0.2	207.0 ± 1.0	93.1 ± 1.6	61.8 ± 2.3	38.6 ± 5.2
2E 1853.7+1534	47.40	6.1	2.5 ± 0.6	3.1 ± 1.4	< 2.8	
IGR J19443+2117	57.79	-1.4	6.2 ± 0.9	2.8 ± 2.1	< 3.9	
Her X-1	58.15	37.5	44.4 ± 1.6	10.5 ± 4.3	< 17.0	
3C382	61.32	17.4	21.1 ± 3.5	11.2 ± 7.2	< 11.3	
KS 1947+300	66.10	2.1	18.9 ± 0.9	9.1 ± 2.2	12.8 ± 4.0	< 17.6
Cyg X-1**	71.33	3.1	811.0 ± 1.1	876.5 ± 1.7	769.9 ± 3.1	500.6 ± 6.9
Cyg A	76.21	5.8	2.8 ± 0.6	< 1.6		
EXO 2030+375	77.14	-1.2	39.0 ± 0.6	15.4 ± 1.5	< 2.8	
Cyg X-3	79.84	0.7	146.2 ± 0.6	56.2 ± 1.5	25.0 ± 2.9	14.8 ± 6.2
SAX J2103.5+4545	87.12	-0.7	11.7 ± 0.6	< 1.6		
Cyg X-2	87.32	-11.3	8.8 ± 0.8	< 2.1		
IGR J21335+5105	94.41	-0.5	11.0 ± 0.8	< 2.2		
4U 2206+543	100.60	-1.1	4.1 ± 0.8	5.1 ± 2.1	11.6 ± 3.7	< 7.6
Cas A	111.71	-2.1	2.6 ± 0.4	3.0 ± 1.1	< 2.2	
709 Cas	120.07	-3.4	3.3 ± 0.4	< 1.2		
γ Cas	123.55	-2.2	3.0 ± 0.5	1.3 ± 1.3	< 2.5	
1A 0114+650	125.71	2.6	6.7 ± 0.6	2.7 ± 1.6	< 3.1	
X0115+63	125.92	1.0	19.8 ± 0.9	8.3 ± 1.3	< 5.2	
4U0142+61	129.38	-0.4	3.3 ± 0.7	2.9 ± 1.7	< 3.0	
GT 0236+610	135.68	1.1	3.6 ± 0.9	4.8 ± 2.4	< 4.5	
MKN3	143.30	22.7	5.9 ± 1.3	7.4 ± 3.7	< 7.0	
V0332+53*	146.05	-2.2	105.4 ± 1.9	11.7 ± 3.1	< 6.0	
NGC 4151	155.08	75.1	28.2 ± 1.4	34.4 ± 3.9	22.9 ± 6.8	46.9 ± 14.1
X Per	163.09	-17.1	22.7 ± 2.6	41.1 ± 6.2	27.7 ± 11.2	< 23.9
NGC1068	172.14	-51.9	4.7 ± 1.2	9.9 ± 3.3	7.7 ± 6.5	

(*) are sources variables on pointing time scale (~ 2500 s in the 25-50 keV band. Cyg X-1(***) is variable up to 200 keV. (+) more than one possible identification (a) Sources are separated in the 20-50 keV band, but may be confused at higher energies.

(b) can be affected by SGR 1806-20.

Note. — The catalog contains only the sources detected in the 50-150 keV band. The counts for diffuse continuum and sources were extracted simultaneously to obtain these data.(**) Source tentatively identified.

Table 2. The best fit parameters for the spectra presented on fig 9

	index1	Ecut	F_{50keV} $\times 10^{-4} ph$ $cm^{-2} s^{-1} keV^{-1}$	index2	F_{50keV} $\times 10^{-4} ph$ $cm^{-2} s^{-1} keV^{-1}$	F_{511keV} $\times 10^{-4} ph$ $cm^{-2} s^{-1}$	F_{posit} $\times 10^{-4} ph$ $cm^{-2} s^{-1}$	f_p
		keV						
Diffuse 1	0 (fixed)	7.5 ± 1	0.66 ± 0.05					
Diffuse 2				1.55 ± 0.25	1.4 ± 0.15			
Diffuse 3						8.68 ± 0.61	36.1 ± 4.2	0.98 ± 0.05
Sources	2.67 ± 0.04		24.7 ± 1.0					

Note. — Diffuse 1 corresponds to the component at low energy, potentially associated with a white dwarf population.
Diffuse 2 corresponds to the "true" diffuse emission, potentially related to the CR particles.
Diffuse 3 corresponds to the annihilation processus.
Sources : a 5% systematic error is added to the combined spectrum.